Nanoscale

PAPER

View Article Online
View Journal

Cite this: DOI: 10.1039/d5nr04551g

Anchored nanocatalysts enable efficient oxygen reduction in barium cobaltite cathodes

InSik Lim,†[a] Hyun Sik Yoo,†[b] DongHwan Oh,[c] Gaon Heo,[a] Seonmin Oh,[a] Bonjae Koo,[d] Wonyoung Lee *[b,e] and Jun Hyuk Kim *[a,e]

Received 29th October 2025,
Accepted 29th March 2026

DOI: 10.1039/d5nr04551g

rsc.li/nanoscale

Solid oxide fuel cells (SOFCs) are hindered by sluggish oxygen reduction reaction (ORR) kinetics at the cathode. Ex-solution, which generates socketed nanoparticles from the perovskite lattice, offers a promising strategy to overcome this limitation but has rarely been applied to cathodes. In this work, $BaCo_{0.8}Ta_{0.2}O_{3-\delta}$ (BCT) was doped with Ag, Cu, and Ni to induce ex-solution under controlled reducing conditions. Structural and microscopic analyses confirmed the formation of socketed nanoparticles on the perovskite surface. Electrochemical measurements showed that ex-solved cathodes exhibited reduced polarization resistance (R_p) compared to their non ex-solved counterparts, with ex-solved BCT–Ag (eBCT–Ag) achieving the lowest R_p (0.0210 Ω cm^2 at 650 °C, ~49% reduction). A single-cell test with eBCT–Ag delivered a maximum power density of ~0.68 W cm^{-2} at 650 °C. These results demonstrate the successful application of ex-solution to SOFC cathodes, providing an effective pathway for high-performance cathode design.

1. Introduction

Climate change and environmental pollution underscore the urgent need for sustainable energy conversion technologies.[1,2] While renewable sources such as solar and wind are rapidly expanding, their intrinsic intermittency limits reliable power supply.[3–5] This challenge highlights the importance of high-efficiency conversion devices, with solid oxide fuel cells (SOFCs) emerging as one of the most promising candidates. SOFCs offer high electrochemical efficiency and fuel flexibility with minimal greenhouse gas emission, making them attractive for next-generation energy systems.[6–11] Nevertheless, their widespread commercialization is still impeded by the sluggish oxygen reduction reaction (ORR) at the cathode, which serves as the rate-determining step of the overall electrochemical process.[12–16] The challenge becomes even more severe as the operating temperature decreases to the intermediate regime, where the ORR kinetics decrease substantially, limiting device performance.

To address this critical challenge, the search for efficient and durable electrocatalysts has been a central research focus.[17–21] One promising approach is the ex-solution. Ex-solution refers to the process where transition metal cations first incorporated into the perovskite (chemical formula: ABO_3) lattice, then ex-solved as nanoparticles under reducing conditions.[22,23] These nanoparticles are partially embedded in the parent oxide (otherwise known as socketed morphology), which provides strong anchoring, enhanced thermal stability, and superior durability compared to conventionally deposited catalysts. Ex-solution has been extensively studied in SOFC anodes, where it effectively suppresses carbon deposition and particle coarsening.[24–34] In contrast, its application to cathodes has long been considered impractical because the oxidizing environment of the cathode is fundamentally incompatible with the reducing conditions typically required for ex-solution. If ex-solution could be realized at the cathode side, it would open a new pathway to simultaneously enhance catalytic activity and stability.[35–37] However, experimental demonstrations remain limited, and the understanding on how ex-solved cathode behaves under oxidizing condition is still insufficient.

In this work, we systematically explore the feasibility of ex-solution in the cathode using $BaCo_{0.8}Ta_{0.2}O_{3-\delta}$ (BCT) as the parent oxide.[38] By doping Ag, Cu, and Ni into BCT and applying controlled reduction treatments, we successfully induced ex-solution and obtained distinct nanoparticle morphologies:

---

[a] Department of Future Energy Engineering, Sungkyunkwan University, Suwon, Republic of Korea. E-mail: jkim765@skku.edu
[b] School of Mechanical Engineering, Sungkyunkwan University, Suwon, Republic of Korea. E-mail: leewy@skku.edu
[c] Department of Chemical and Biomolecular Engineering (BK21 Four), Korea Advanced Institute of Science and Technology (KAIST), Daejeon 34141, Republic of Korea
[d] School of Chemistry and Energy, Sungshin Women's University, Seoul, Republic of Korea
[e] SKKU Institute of Energy Science and Technology (SIEST), Sungkyunkwan University, Suwon, Republic of Korea

† These authors contributed equally.

Ag and Cu emerged as individual metallic nanoparticles co-exsolved with Co, whereas Ni formed alloyed particles with Co. These nanoparticles were uniformly distributed on the electrode surface, providing additional active sites that enhanced the ORR kinetics. Electrochemical analyses confirmed a reduction of polarization resistance by up to ~49% and measurable improvements in single-cell performance. This study demonstrates the effectiveness of incorporating multiple transition-metal dopants to enable ex-solution-based catalyst design, thereby offering a practical strategy for the development of advanced SOFC cathodes.

2. Results and discussion

2.1 Physical characterization of the materials

In this study, $BaCo_{0.8}Ta_{0.2}O_{3-\delta}$ (BCT) was selected as the parent cathode material. BCT exhibits high ORR activity and has recently attracted attention as a promising candidate for next-generation SOFC cathodes. Moreover, its perovskite structure provides excellent compositional flexibility, enabling the incorporation of various transition-metal dopants. Ag, Cu, and Ni were chosen as dopants considering both catalytic activity[39] and economic feasibility,[40] and A-site deficiency was introduced to effectively promote ex-solution.

X-ray diffraction (XRD) patterns confirmed that all $Ba_{0.95}Co_{0.8}Ta_{0.2}O_{3-\delta}$–$Ag_{0.05}$ (BCT–Ag), $BaCo_{0.8}Ta_{0.2}O_{3-\delta}$–$Cu_{0.05}$ (BCT–Cu), and $BaCo_{0.8}Ta_{0.2}O_{3-\delta}$–$Ni_{0.05}$ (BCT–Ni) samples maintained a single-phase cubic perovskite structure with $Pm\bar{3}m$ space group (Fig. 1a and Fig. S1–S3). Lattice parameter analysis revealed that BCT–Ag exhibited a slightly decreased lattice constant (a = 4.0715 Å) compared to BCT (a = 4.078 Å), whereas BCT–Ni and BCT–Cu showed increased values (a = 4.0864 Å and a = 4.0883 Å, respectively). These variations are attributed to the differences in ionic radii of the dopant cations. Specifically, the ionic radii follow the order Ba^{2+} (161 pm) > Ag^{+} (115 pm) ≫ Cu^{2+} (73 pm) > Ni^{2+} (69 pm) > Ta^{5+} (64 pm) > Co^{3+} (61 pm), which is consistent with the observed trend in lattice parameter changes. These results suggest that Ag is incorporated at the A-site, while Cu and Ni occupy the B-site, confirming the successful substitution of the dopant cations into the perovskite lattice. Raman spectra of all samples displayed a distinct A_{1g} breathing mode at approximately 670 cm^{-1}, which corresponds to the vibration of BO_6 octahedra, indicating the retention of the cubic perovskite structure (Fig. 1b). In addition, the characteristic peak near 600 cm^{-1} inherent to hexagonal $BaCoO_{2.6}$ (BCO) was absent, further supporting that all synthesized samples were obtained as a single cubic perovskite phase.[41]

Jun Hyuk Kim

Jun Hyuk Kim received his Ph.D. degree from Georgia Institute of Technology (Georgia Tech) and served as a post-doctoral researcher at Korea Advanced Institute of Science & Technology (KAIST). He is currently an assistant professor in the department of future energy engineering at Sungkyunkwan University (SKKU), Republic of Korea. Dr Kim's primary research interests focus on sustainable energy conversion and catalysis. His current research activities include: (1) development of high-performance solid oxide/protonic ceramic fuel cells and electrolysis cells, (2) ex-solution catalysts and (3) in situ and operando Raman characterization of gas-solid interfaces.

To find safe ex-solution temperature window with minimal damage inflicted on the host structure, samples were investigated using H_2-temperature programmed reduction (H_2-TPR) under 10% H_2/Ar condition. The results revealed distinct reduction onset temperatures for the doped samples, with the main reduction peaks observed at 358 °C, 312 °C, and 388 °C for Ag-doped, Cu-doped and Ni-doped samples, respectively (Fig. 1c and Fig. S4). Both doped and undoped BCT samples described a major reduction peak around 530 °C, which indicates the reduction of Co at this temperature. Thereby the reduction tendency can be written as follows: Cu (312 °C) > Ag (358 °C) > Ni (388 °C) > Co (530 °C). Therefore, to achieve ex-solution while minimizing the host disruption, 400 °C was selected as the reduction condition to promote ex-solution in all samples.

Thereafter, ex-solution was carried out by treating the Ag-, Cu-, and Ni-doped perovskite samples in a quartz tube under flowing 4% H_2/Ar at 400 °C. Scanning electron microscopy (SEM) images were collected to compare the surface morphology before and after reduction (Fig. 1d, f, h and Fig. S5–S7). After reduction, uniformly distributed nanoparticles were observed on the electrode surfaces of BCT–Cu (after 3 h) and BCT–Ag (after 5 h), exhibiting a socketed morphology. We found that BCT–Ni requires a longer reduction time (20 h) to nucleate and grow nanoparticles which is consistent with the relatively high Ni reduction onset temperature observed in previous H_2-TPR results. The corresponding nanoparticle densities were estimated as ~391, ~589, and ~221 particles per μm^2 for ex-solved BCT–Ag (eBCT–Ag), ex-solved BCT–Cu (eBCT–Cu), and ex-solved BCT–Ni (eBCT–Ni), respectively (see Fig. S8 for detailed analysis).

High-angle annular dark field scanning transmission electron microscope (HAADF-STEM) analysis was performed to elucidate the morphology and composition of the ex-solved nanoparticles (Fig. 1e, g and i). We found not only the ex-solution of Ag, Cu and Ni, but also ex-solution of some Co. Particularly, Ag and Cu were ex-solved as independent metallic nanoparticles separated from Co nanoparticles, whereas Ni formed alloyed nanoparticles with Co. This distinct ex-solution behavior can be rationalized based on the solid-state miscibility between Co and each dopant metal, as reflected in their respective binary phase diagrams. According to the Ag–Co[42] and Cu–Co phase diagrams,[43] both systems exhibit extremely

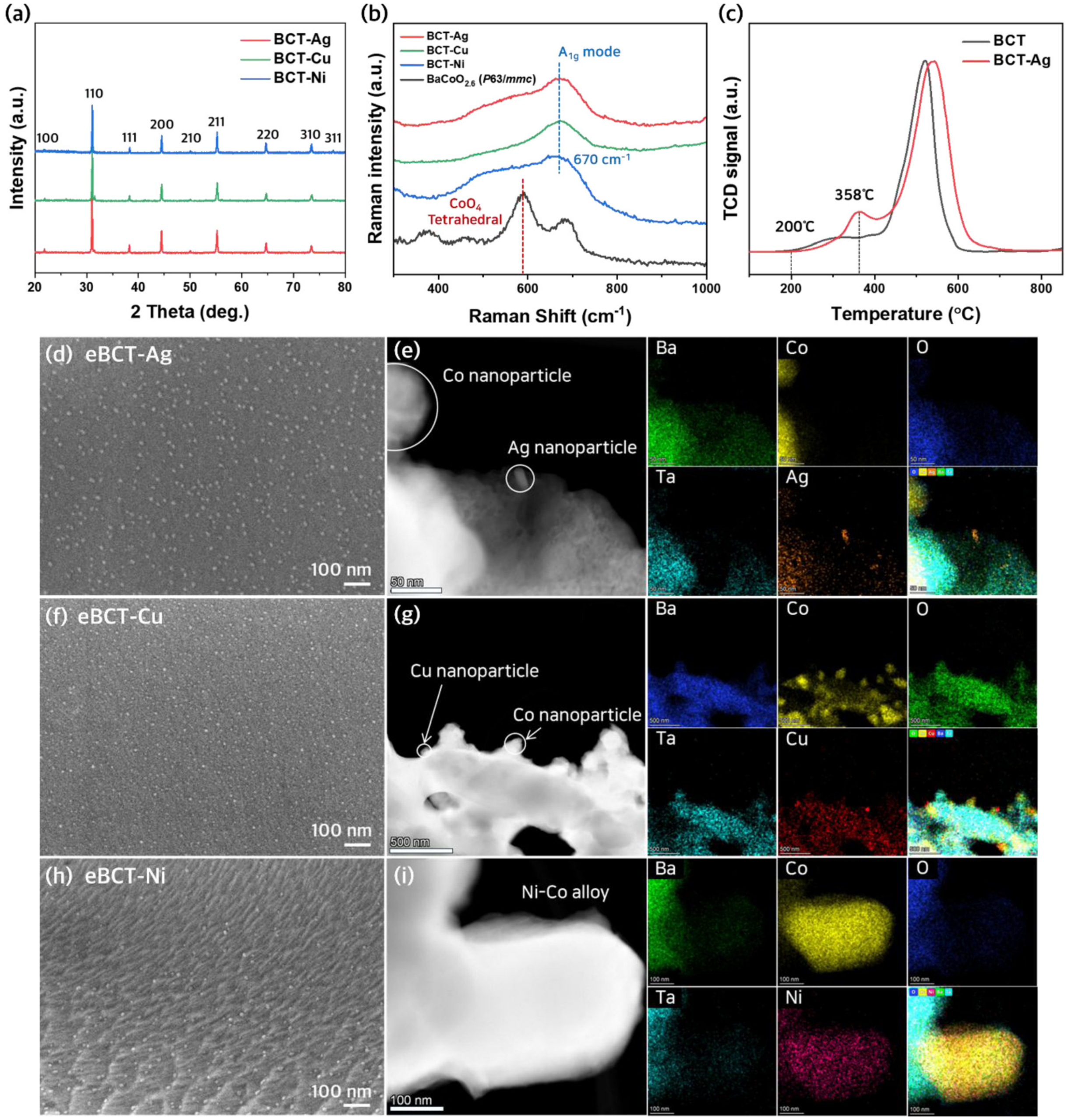

Fig. 1 Physical characterization of the synthesized $Ba_{0.95}Co_{0.8}Ta_{0.2}O_{3-\delta}$–$Ag_{0.05}$ (BCT–Ag), $BaCo_{0.8}Ta_{0.2}O_{3-\delta}$–$Cu_{0.05}$ (BCT–Cu), and $BaCo_{0.8}Ta_{0.2}O_{3-\delta}$–$Ni_{0.05}$ (BCT–Ni): (a) X-ray diffraction (XRD) patterns of as-synthesized powders, and (b) Raman spectra of as-synthesized powders compared with hexagonal $BaCoO_{2.6}$ (BCO). (c) H_2-temperature programmed reduction (H_2-TPR) data of BCT–Ag compared with $BaCo_{0.8}Ta_{0.2}O_{3-\delta}$ (BCT), scanning electron microscopy (SEM) images after reduction treatment under 4% H_2/Ar at 400 °C: (d) BCT–Ag after 5 hours, (f) BCT–Cu after 5 hours, (h) BCT–Ni after 20 hours, and corresponding transmission electron microscope (TEM) images and energy-dispersive X-ray spectroscopy (EDX) analysis are presented in (e), (g), and (i), respectively.

limited mutual solubility near 400 °C, favoring phase separation and thereby leading to the formation of discrete metallic nanoparticles upon ex-solution. In contrast, the Ni–Co phase diagram[44] shows a broad solid-solution region at similar temperatures, rendering Ni–Co alloy formation thermodynamically favorable once reduced species become mobile at the surface. These thermodynamic considerations are consistent with previous reports of Ni–Co alloy nanoparticle formation.[45,46] Nonetheless, these results confirm that ex-solution of metal nanocatalysts was successfully achieved on BCT mother oxide.

2.2 Electrochemical performance evaluation

Electrochemical performance spectroscopy (EIS) was performed using symmetric cells to evaluate the ORR catalytic activity of eBCT–Ag, eBCT–Cu and eBCT–Ni cathodes (Fig. 2). The symmetrical cells were fabricated with a cathode|electro-

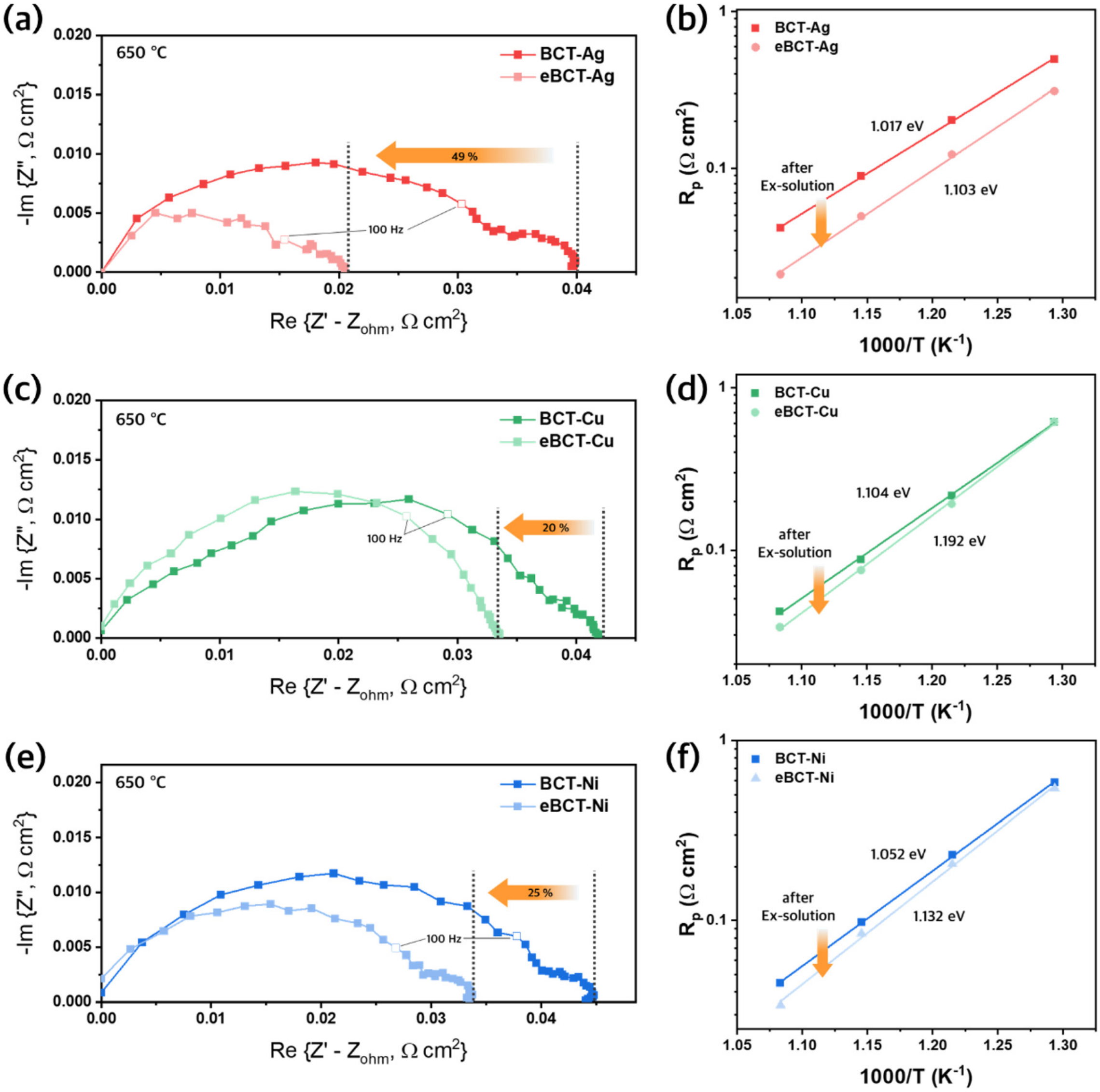

Fig. 2 Electrochemical impedance spectroscopy (EIS) profiles: (a) $Ba_{0.95}Co_{0.8}Ta_{0.2}O_{3-\delta}$–$Ag_{0.05}$ (BCT–Ag) and ex-solved BCT–Ag (eBCT–Ag), (c) $BaCo_{0.8}Ta_{0.2}O_{3-\delta}$–$Cu_{0.05}$ (BCT–Cu) and ex-solved BCT–Cu (eBCT–Cu), (e) $BaCo_{0.8}Ta_{0.2}O_{3-\delta}$–$Ni_{0.05}$ (BCT–Ni) and ex-solved BCT–Ni (eBCT–Ni) in symmetric cell configurations (electrode|$Sm_{0.2}Ce_{0.8}O_{2-\delta}$ (SDC)|electrode). Corresponding Arrhenius plots of the polarization curves: (b) BCT–Ag and eBCT–Ag, (d) BCT–Cu and eBCT–Cu, (f) BCT–Ni and eBCT–Ni, respectively.

lyte|cathode configuration, employing $Sm_{0.2}Ce_{0.8}O_{2-\delta}$ (SDC) as the electrolyte. All measurements were conducted at an oxygen partial pressure (pO_2) of 0.21 atm over the temperature range of 500–650 °C, and the corresponding Nyquist and Arrhenius plots are presented in Fig. S12–S14. The results showed that all ex-solved samples exhibited reduced polarization resistance (R_p) compared to pristine samples, with R_p values of 0.0210, 0.0336, and 0.0337 Ω cm^2 for eBCT–Ag, eBCT–Cu and eBCT–Ni, respectively. Among them, eBCT–Ag demonstrated the most significant improvement, with an ~49% reduction in R_p. The R_p values of eBCT–Ag were measured to be 0.0210, 0.0494, 0.123, and 0.310 Ω cm^2 at 650, 600, 550, and 500 °C, respectively. The superior performance of eBCT–Ag over Cu and Ni-doped samples can be ascribed to excellent ORR activity of Ag, as implied by the volcano plot provided by Nørskov *et al.*[39] According to Sabatier's principle, the bond strength between adsorbed species and the surface plays a critical role in catalytic activity, and to achieve the optimal catalytic performance, binding energies on the catalyst surface should be moderate. As reported by Nørskov *et al.*, the calculated oxygen adsorption energies (ΔE_O) on Ag, Cu and Ni surfaces are approximately 2.12, 1.20 and 0.34 eV, respectively. As such, oxygen binds to the Ag surface with an intermediate strength, while Cu and Ni are too strong. Indeed, the positive ORR promotion driven by Ag has frequently reported in SOFC fields.[35,37,47,48]

A performance map comparing the ORR activities of the developed eBCT–Ag with several benchmark materials is presented in the Fig. S15 and Table S1.[49–53] As shown, the electrode polarization resistance of eBCT–Ag is lower or comparable with previously reported cathodes, indicating the promising electrochemical performance of the developed ex-solution derived cathodes.

While the reduced R_p clearly demonstrates the beneficial effect of ex-solution, the Nyquist plots alone do not resolve which elementary electrode processes are predominantly accelerated. Because the overall impedance arc typically comprises multiple electrochemical processes operating over different time scales, a more quantitative deconvolution is required to identify the origin of the performance enhancement. To this end, distribution of relaxation times (DRT) analysis was employed for detailed interpretation of the EIS spectra (Fig. 3b–d). The DRT spectra reveal three well-defined peaks corresponding to the high-frequency (HF, 10^3–10^5 Hz), mid-frequency (MF, 10^2–10^3 Hz), and low-frequency (LF, ~10^{-1}–10^2 Hz) regions. The HF peak is generally attributed to charge transfer across the electrode/electrolyte interface, the MF peak to surface oxygen adsorption and exchange processes, and the LF peak to mass transport processes such as gas-phase diffusion.[54,55] To validate these assignments, pO_2-dependent DRT measurements were performed at 650 °C with pO_2 systematically varied from 0.1 to 1 atm (Fig. 3e, f and Fig. S16). The MF and LF peaks exhibited pronounced suppression with increasing pO_2, demonstrating their strong involvement in oxygen related reaction process. Quantitative analysis of the resistance contributions ($\log R_p$ *vs.* $\log pO_2$) yielded reaction orders of $n \approx 0.5$ for the MF process and $n \approx 1$ for the LF process (Fig. 3g and Fig. S17). These values are consistent with oxygen surface exchange and diffusion-related processes, respectively, according to established kinetic models for mixed ionic–electronic conducting cathodes.[56]

Importantly, compared to the pristine sample, all ex-solved electrodes exhibited noticeable reductions in resistance across

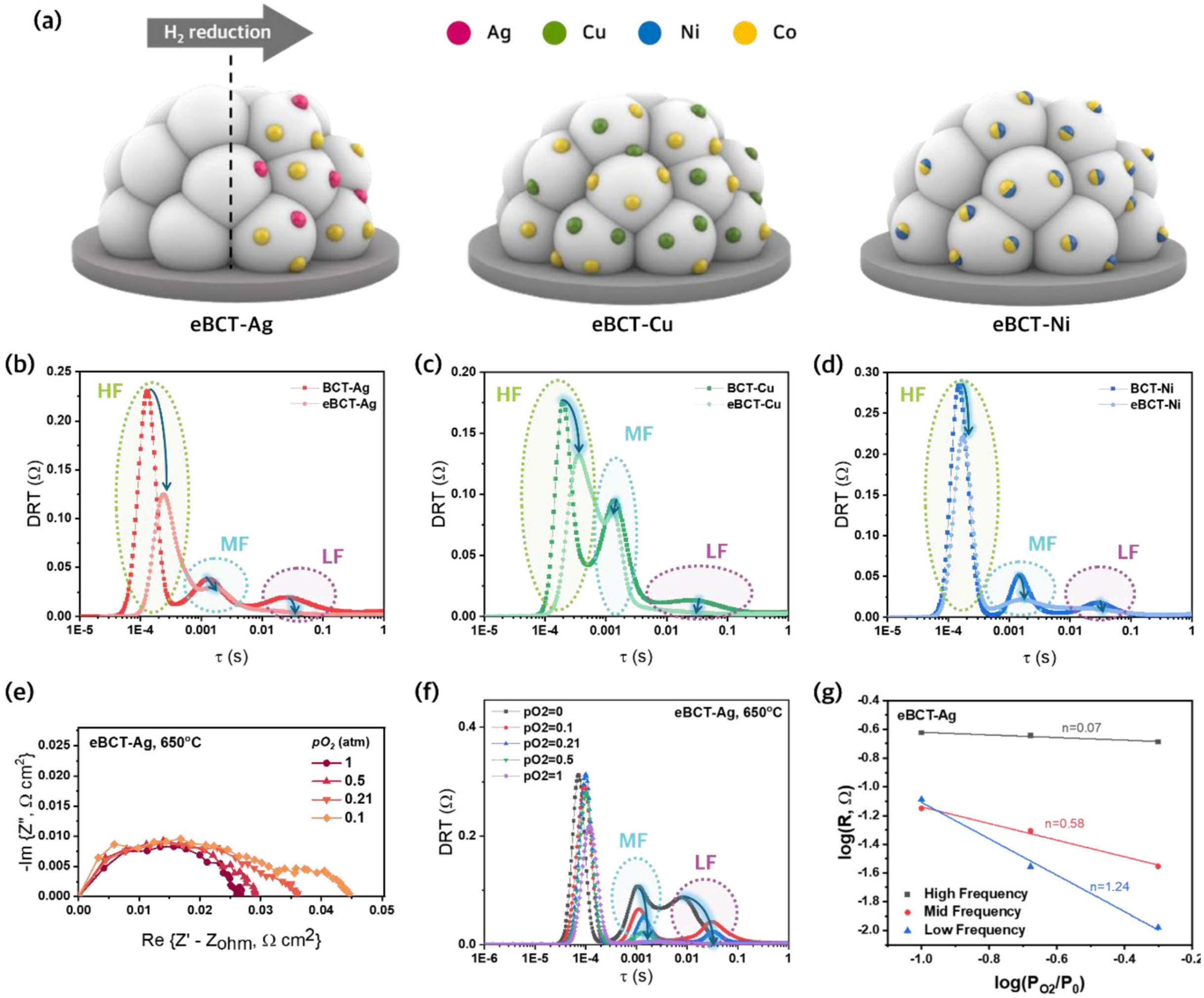

Fig. 3 (a) Schematic of ex-solved $Ba_{0.95}Co_{0.8}Ta_{0.2}O_{3-\delta}$–$Ag_{0.05}$ (eBCT–Ag), ex-solved $BaCo_{0.8}Ta_{0.2}O_{3-\delta}$–$Cu_{0.05}$ (eBCT–Cu), and ex-solved $BaCo_{0.8}Ta_{0.2}O_{3-\delta}$–$Ni_{0.05}$ (eBCT–Ni). Distribution of relaxation times (DRT) analysis of (b) BCT–Ag and eBCT–Ag, (c) BCT–Cu and eBCT–Cu, (d) BCT–Ni and eBCT–Ni. (e) Electrochemical impedance spectroscopy (EIS) of eBCT–Ag oxygen electrode at 650 °C measured with $Sm_{0.2}Ce_{0.8}O_{2-\delta}$ (SDC) symmetric cells in dry air (pO_2 = 0.1–1 atm), (f) corresponding DRT analysis and (g) corresponding oxygen partial pressure dependency outcomes of HF, MF and LF.

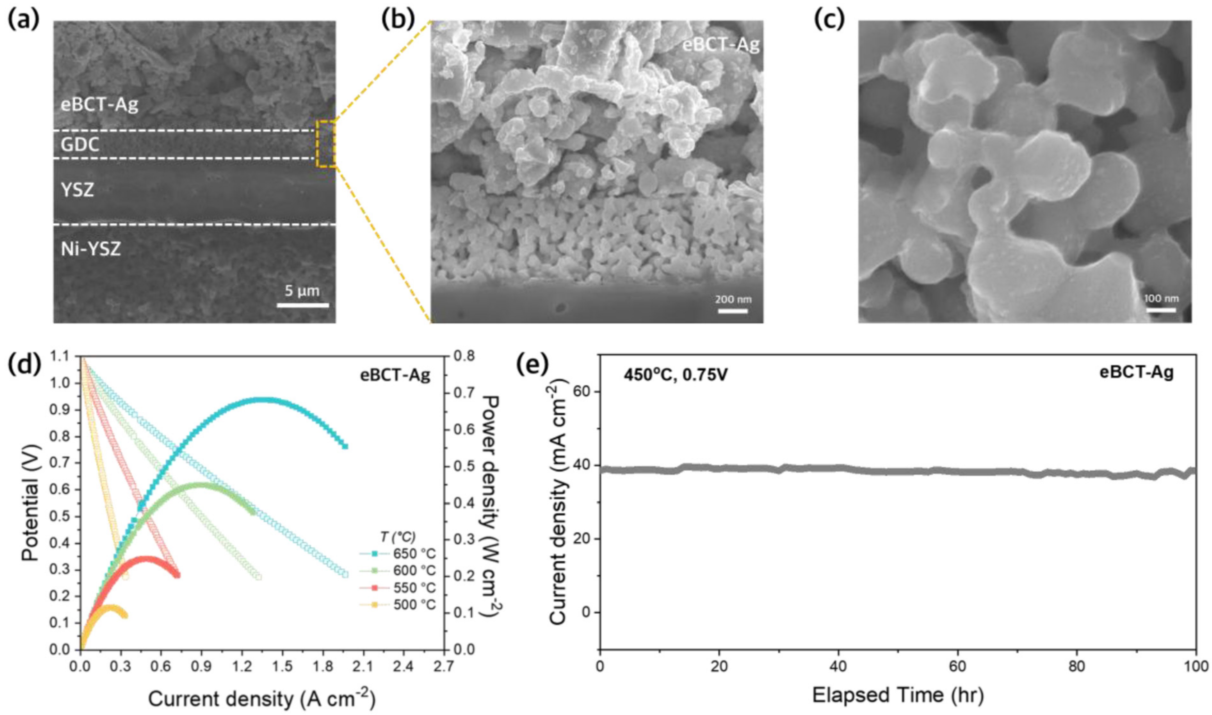

Fig. 4 Performance demonstration with single cell: (a) cross-sectional SEM image of single cell with configuration of Ni-yttria-stabilized zirconia (YSZ) anode|YSZ electrolyte|$Gd_{0.1}Ce_{0.9}O_{2-\delta}$ (GDC) interlayer|ex-solved $Ba_{0.95}Co_{0.8}Ta_{0.2}O_{3-\delta}$–$Ag_{0.05}$ (eBCT–Ag) cathode, (b) magnified SEM image of the eBCT–Ag cathode and GDC interlayer interface, showing no delamination between the two layers, (c) surface morphology of the eBCT–Ag cathode after operation, (d) *I*–*V*–*P* curve of a single cell with eBCT–Ag cathode, (e) long-term stability data measured with eBCT–Ag cathode at 450 °C in dry air (pO_2 = 0.21 atm).

the HF, MF, and LF regions (Fig. 3b–d). This observation indicates that ex-solution globally accelerates the ORR pathway rather than selectively improving a single kinetic step. Collectively, these results provide mechanistic evidence that the ex-solved nanoparticles enhance oxygen surface exchange kinetics while simultaneously alleviating diffusion-related limitations, thereby accelerating both interfacial and mass transport processes that govern the overall ORR performance.

2.3 Demonstration with single cell

Next, we evaluated our developed cathode materials in a button cell configuration, simulating a realistic SOFC operation. Amongst all samples, eBCT–Ag exhibited the best performance in the half-cell tests, thereby a representative single cell data is shown in Fig. 4. The results for the other cathode materials were also obtained and are shown in Fig. S18. The cell consisted of Ni-yttria-stabilized zirconia (YSZ) anode, YSZ electrolyte, $Gd_{0.1}Ce_{0.9}O_{2-\delta}$ (GDC) interlayer, and eBCT–Ag cathode. Humidified H_2 was supplied to the anode as fuel, while air was fed to the cathode side during the measurements. As shown in the *I*–*V*–*P* curves, the single cell delivered a maximum power density of ~0.68 W cm^{-2} at 650 °C, demonstrating promising electrochemical performance (Fig. 4d). Furthermore, long-term stability test at 450 °C demonstrates that the cell maintains stable performance over approximately 100 h without noticeable degradation (Fig. 4e). Additional short-term stability test at 650 °C for 50 h (Fig. S19) further confirm the robustness of the ex-solved cathode under more demanding conditions.

Post-test SEM analysis was also performed to investigate the structural integrity of the operated cell (Fig. 4a). No delamination was observed between the electrolyte and electrodes, indicating that the overall cell architecture was well maintained after operation (Fig. 4b). Furthermore, the ex-solved Ag nanoparticles were stably retained on the cathode surface (Fig. 4c), confirming their structural stability after operation. Overall, these results demonstrate that the ex-solution strategy was successfully implemented in the cathode and effectively applied to SOFC single cell, providing experimental evidence of its potential for practical high-performance cathode design.

3. Conclusion

In this study, $BaCo_{0.8}Ta_{0.2}O_{3-\delta}$ (BCT) was employed as the parent oxide to apply the ex-solution strategy to SOFC cathodes, and Ag, Cu, and Ni were doped to systematically investigate their ex-solution behavior and electrochemical performance. Among the three, Ag ex-solution delivered the most pronounced enhancement, followed by Cu and Ni. Ag and Cu nanoparticles were ex-solved as discrete metallic phases with Co, while Ni formed Ni–Co alloy nanoparticles. In all cases, ex-solution markedly altered the ORR pathways, thereby enhancing the reaction kinetics. Notably, eBCT–Ag achieved a polarization resistance as low as 0.0210 Ω cm^2 at 650 °C through synergistic interplay between ex-solved nanoparticles and host lattice. These findings establish ex-solution as a versatile strategy for boosting SOFC cathode activity and highlight its broader potential to revisit and optimize other perovskite materials through controlled nanoparticle ex-solution.

Author contributions

W. L. and J. H. K. conceived and supervised the project. IS. L. designed the material compositions and performed the following experiments: material synthesis, H_2-TPR, SEM, half-cell measurements, and DRT. H. S. Y. performed single cell tests. DH.O. conducted TEM analysis. G. H. assisted in material preparation and characterization. S. O. performed Raman analysis. B. K. conducted XRD analysis. IS. L., H. S. Y., W. L. and J. H. K. contributed to the writing of the manuscript.

Conflicts of interest

There are no conflicts to declare.

Data availability

All data generated or analyzed during this study are included in this published article and its supplementary information (SI). Supplementary information is available. See DOI: https://doi.org/10.1039/d5nr04551g.

Acknowledgements

This research was supported by Korea Electric Power Corporation (Grant number: R23XO07-02). This work was supported by the National Research Foundation of Korea (NRF) grant funded by the Korea government (MSIT) (2022R1A2C3012372).

References

1 D. P. van Vuuren, *et al.*, Energy, land-use and greenhouse gas emissions trajectories under a green growth paradigm, *Glob. Environ. Change*, 2017, **42**, 237–250.

2 D. Gielen, *et al.*, The role of renewable energy in the global energy transformation, *Energy Strat. Rev.*, 2019, **24**, 38–50.

3 I. Energy Agency, *Net Zero by 2050 - A Roadmap for the Global Energy Sector*, 2050, https://www.iea.org/t&c/.

4 Q. Hou, *et al.*, Probabilistic duck curve in high PV penetration power system: Concept, modeling, and empirical analysis in China, *Appl. Energy*, 2019, **242**, 205–215.

5 M. Obi and R. Bass, Trends and challenges of grid-connected photovoltaic systems - A review, *Renewable Sustainable Energy Rev.*, 2016, **58**, 1082–1094, DOI: 10.1016/j.rser.2015.12.289 preprint at.

6 Y. Chen, *et al.*, A robust fuel cell operated on nearly dry methane at 500 °C enabled by synergistic thermal catalysis and electrocatalysis, *Nat. Energy*, 2018, **3**, 1042–1050.

7 Z. Gao, L. V. Mogni, E. C. Miller, J. G. Railsback and S. A. Barnett, A perspective on low-temperature solid oxide fuel cells, *Energy Environ. Sci.*, 2016, **9**, 1602–1644, DOI: 10.1039/c5ee03858h preprint at.

8 Z. Li, *et al.*, High-entropy cathodes with Cr and CO_2 tolerance via the combination of $Ba_{0.5}Sr_{0.5}Co_{0.8}Fe_{0.2}O_{3-\delta}$ and Nd, Ni, Zr ternary doping for both oxygen ion and proton conducting solid oxide fuel cells, *Adv. Compos. Hybrid Mater.*, 2025, **8**, 87.

9 Y. Liao, *et al.*, An active high-entropy air electrode for enhanced reversible solid oxide cell performance and stability, *Mater. Rep.: Energy*, 2025, **5**, 100381.

10 M. Xiao, *et al.*, High-entropy strategies transforming solid oxide cells: Progress and perspectives, *Mater. Rep.: Energy*, 2025, 100400, DOI: 10.1016/j.matre.2025.100400.

11 Y. Jiang, F. Li, B. Ma and Z. Gao, Solid Oxide Fuel Cells Fed with Heavy-Duty Diesel Fuels: Advances, Challenges, and Perspectives in Power Generation, *Renewables*, 2025, **3**, 267–305.

12 C. Pellegrinelli, Y.-L. Huang, J. A. Taillon, L. G. Salamanca-Riba and E. D. Wachsman, A Study of SOFC Cathode Degradation in H_2O Environments, *ECS Trans.*, 2014, **64**, 17–28.

13 B. Hu, M. Keane, M. K. Mahapatra and P. Singh, Stability of strontium-doped lanthanum manganite cathode in humidified air, *J. Power Sources*, 2014, **248**, 196–204.

14 J. S. Hardy, *et al.*, Evaluation of cation migration in lanthanum strontium cobalt ferrite solid oxide fuel cell cathodes: Via in-operando X-ray diffraction, *J. Mater. Chem. A*, 2018, **6**, 1787–1801.

15 Y. Chen, *et al.*, Impact of Sr segregation on the electronic structure and oxygen reduction activity of $SrTi_{1-x}Fe_xO_3$ surfaces, *Energy Environ. Sci.*, 2012, **5**, 7979–7988.

16 P. Hjalmarsson, M. Søgaard and M. Mogensen, Electrochemical performance and degradation of $(La_{0.6}Sr_{0.4})_{0.99}CoO_{3-\delta}$ as porous SOFC-cathode, *Solid State Ion.*, 2008, **179**, 1422–1426.

17 H. Zhang, *et al.*, Surface Regulating of a Double-Perovskite Electrode for Protonic Ceramic Fuel Cells to Enhance Oxygen Reduction Activity and Contaminants Poisoning Tolerance, *Adv. Energy Mater.*, 2022, **12**, 2200761.

18 H. Lee, *et al.*, Enhanced Electrochemical Performance and Durability of the $BaCo_{0.4}Fe_{0.4}Zr_{0.1}Y_{0.1}O_{3-\delta}$ Composite Cathode of Protonic Ceramic Fuel Cells via Forming Nickel Oxide Nanoparticles, *ACS Appl. Energy Mater.*, 2021, **4**, 11564–11573.

19 X. Lu, *et al.*, A cobalt-free Pr_6O_{11}–$BaCe_{0.2}Fe_{0.8}O_{3-\delta}$ composite cathode for protonic ceramic fuel cells with promising oxygen reduction activity and hydration ability, *J. Power Sources*, 2024, **599**, 234233.

20 M. Saqib, *et al.*, Modification of Oxygen-Ionic Transport Barrier of $BaCo_{0.4}Zr_{0.1}Fe_{0.4}Y_{0.1}O_3$ Steam (Air) Electrode by Impregnating Samarium-Doped Ceria Nanoparticles for Proton-Conducting Reversible Solid Oxide Cells, *J. Electrochem. Soc.*, 2019, **166**, F746–F754.

21 B. Liu, L. Jia, B. Chi, J. Pu and J. Li, A novel $PrBaCo_2O_{5+\sigma}$-$BaZr_{0.1}Ce_{0.7}Y_{0.1}Yb_{0.1}O_3$ composite cathode for proton-conducting solid oxide fuel cells, *Composites, Part B*, 2020, **191**, 107936.

22 D. Neagu, *et al.*, Nano-socketed nickel particles with enhanced coking resistance grown in situ by redox exsolution, *Nat. Commun.*, 2015, **6**, 8120.

23 D. Neagu, G. Tsekouras, D. N. Miller, H. Ménard and J. T. S. Irvine, In situ growth of nanoparticles through control of non-stoichiometry, *Nat. Chem.*, 2013, **5**, 916–923.

24 Y. Gao, D. Chen, M. Saccoccio, Z. Lu and F. Ciucci, From material design to mechanism study: Nanoscale Ni exsolution on a highly active A-site deficient anode material for solid oxide fuel cells, *Nano Energy*, 2016, **27**, 499–508.

25 C. Duan, *et al.*, Highly durable, coking and sulfur tolerant, fuel-flexible protonic ceramic fuel cells, *Nature*, 2018, **557**, 217–222.

26 B. Hua, M. Li, Y. F. Sun, J. H. Li and J. L. Luo, Enhancing Perovskite Electrocatalysis of Solid Oxide Cells Through Controlled Exsolution of Nanoparticles, *ChemSusChem*, 2017, **10**, 3333–3341, DOI: 10.1002/cssc.201700936 preprint at.

27 Y. Sun, *et al.*, A-site deficient perovskite: The parent for in situ exsolution of highly active, regenerable nano-particles as SOFC anodes, *J. Mater. Chem. A*, 2015, **3**, 11048–11056.

28 K. J. Kim, *et al.*, A Highly Active and Redox-Stable $SrGdNi_{0.2}Mn_{0.8}O_{4\pm\delta}$ Anode with in Situ Exsolution of Nanocatalysts, *ACS Catal.*, 2019, **9**, 1172–1182.

29 T. Zhu, H. E. Troiani, L. V. Mogni, M. Han and S. A. Barnett, Ni-Substituted $Sr(Ti,Fe)O_3$ SOFC Anodes: Achieving High Performance via Metal Alloy Nanoparticle Exsolution, *Joule*, 2018, **2**, 478–496.

30 J. J. Lee, *et al.*, *In situ* exsolution of Ni nanoparticles to achieve an active and stable solid oxide fuel cell anode catalyst on A-site deficient $La_{0.4}Sr_{0.4}Ti_{0.94}Ni_{0.06}O_{3-\delta}$, *J. Ind. Eng. Chem.*, 2021, **103**, 264–274.

31 X. Xiong, *et al.*, Slightly ruthenium doping enables better alloy nanoparticle exsolution of perovskite anode for high-performance direct-ammonia solid oxide fuel cells, *J. Mater. Sci. Technol.*, 2022, **125**, 51–58.

32 S. Liu, K. T. Chuang and J. L. Luo, Double-Layered Perovskite Anode with in Situ Exsolution of a Co-Fe Alloy to Cogenerate Ethylene and Electricity in a Proton-Conducting Ethane Fuel Cell, *ACS Catal.*, 2016, **6**, 760–768.

33 O. Kwon, *et al.*, Exsolution trends and co-segregation aspects of self-grown catalyst nanoparticles in perovskites, *Nat. Commun.*, 2017, **8**, 15967.

34 K. Hong, *et al.*, Direct methane protonic ceramic fuel cells with self-assembled Ni-Rh bimetallic catalyst, *Nat. Commun.*, 2023, **14**, 7485.

35 J. H. Kim, *et al.*, Ex-Solved Ag Nanocatalysts on a Sr-Free Parent Scaffold Authorize a Highly Efficient Route of Oxygen Reduction, *Adv. Funct. Mater.*, 2020, **30**, 2001326.

36 S. H. Jeon, *et al.*, Concurrent Amorphization and Nanocatalyst Formation in Cu-Substituted Perovskite Oxide Surface: Effects on Oxygen Reduction Reaction at Elevated Temperatures, *Adv. Mater.*, 2024, **36**, 2404103.

37 Y. Zhu, *et al.*, Promotion of Oxygen Reduction by Exsolved Silver Nanoparticles on a Perovskite Scaffold for Low-Temperature Solid Oxide Fuel Cells, *Nano Lett.*, 2016, **16**, 512–518.

38 J. H. Kim, *et al.*, An universal oxygen electrode for reversible solid oxide electrochemical cells at reduced temperatures, *Energy Environ. Sci.*, 2023, **16**, 3803–3814.

39 J. K. Nørskov, *et al.*, Origin of the overpotential for oxygen reduction at a fuel-cell cathode, *J. Phys. Chem. B*, 2004, **108**, 17886–17892.

40 Rare Earth Price Today | Rare Earth Spot Price Chart | Historical Price of Rare Earth - Shanghai Metal Market. https://www.metal.com/en/markets/33.

41 A. Glamazda, *et al.*, Structural instability of the CoO_4 tetrahedral chain in $SrCoO_{3-\delta}$ thin films, *J. Appl. Phys.*, 2015, **118**, 085313.

42 W. J. Zhu, H. S. Liu, J. S. Wang, H. Q. Dong and Z. P. Jin, Thermodynamic assessment of the Sn-Ag-Co system and solidification simulation of the ternary alloy, *J. Alloys Compd.*, 2009, **481**, 503–508.

43 T. Nishizawa and K. Ishida, The Co-Cu (Cobalt-Copper) System, *Bull. Alloy Phase Diagrams*, 1984, **5**, 161–165.

44 P. (Philip) Nash, *Phase diagrams of binary nickel alloys*, 1991, https://cir.nii.ac.jp/crid/1970023484896599448.

45 Z. Li, L. Cui, J. Luo, J. Li and Y. Sun, Perovskite Chromite With *In situ* Assembled Ni-Co Nano-Alloys: A Potential Bifunctional Electrode Catalyst for Solid Oxide Cells, *Front. Chem.*, 2021, **8**, 595608.

46 H. Ren, *et al.*, In situ exsolution of Ni–Co alloys from A-site-deficient perovskite for efficient ammonia decomposition, *Int. J. Hydrogen Energy*, 2024, **96**, 385–395.

47 J. H. Kim, *et al.*, Water as a hole-predatory instrument to create metal nanoparticles on triple-conducting oxides, *Energy Environ. Sci.*, 2021, **15**, 1097–1105.

48 S. Ahn, *et al.*, Promotion of Reversible Fuel-Power Generation in Protonic Ceramic Electrochemical Cell via Water-Mediated Ex-Solution, *ACS Energy Lett.*, 2025, **10**, 4948–4956.

49 J. H. Kim, *et al.*, Promotion of oxygen reduction reaction on a double perovskite electrode by a water-induced surface modification, *Energy Environ. Sci.*, 2021, **14**, 1506–1516.

50 C. Duan, D. Hook, Y. Chen, J. Tong and R. O'Hayre, Zr and Y co-doped perovskite as a stable, high performance cathode for solid oxide fuel cells operating below 500 °C, *Energy Environ. Sci.*, 2017, **10**, 176–182.

51 Y. Song, *et al.*, A Cobalt-Free Multi-Phase Nanocomposite as Near-Ideal Cathode of Intermediate-Temperature Solid Oxide Fuel Cells Developed by Smart Self-Assembly, *Adv. Mater.*, 2020, **32**, 1906979.

52 Z. Shao and S. M. Halle, A high-performance cathode for the next generation of solid-oxide fuel cells, *Nature*, 2004, **431**, 170–173.

53 C. Yao, *et al.*, A highly active and durable iron-based high-entropy perovskite cathode for solid oxide fuel cells, *J. Energy Chem.*, 2025, **110**, 558–570.

54 Y. Chen, *et al.*, A Highly Efficient Multi-phase Catalyst Dramatically Enhances the Rate of Oxygen Reduction, *Joule*, 2018, **2**, 938–949.

55 Y. Song, *et al.*, Nanocomposites: A New Opportunity for Developing Highly Active and Durable Bifunctional Air Electrodes for Reversible Protonic Ceramic Cells, *Adv. Energy Mater.*, 2021, **11**, 2101899.

56 A. Ndubuisi, S. Abouali, K. Singh and V. Thangadurai, Recent advances, practical challenges, and perspectives of intermediate temperature solid oxide fuel cell cathodes, *J. Mater. Chem. A*, 2022, **10**, 2196–2227.